Available on CMS information server

CMS NOTE 2006-142

The Compact Muon Solenoid Experiment

CMS Note

Mailing address: CMS CERN, CH-1211 GENEVA 23, Switzerland

First performance studies of a prototype for the CASTOR forward calorimeter at the CMS experiment

X. Aslanoglou[3], A. Cyz[4], N. Davis[1], D. d'Enterria[6], E. Gladysz-Dziadus[4], C. Kalfas[2], Y. Musienko[5], A. Kuznetsov[5], A. D. Panagiotou[1]

[1]*University of Athens, Hellas*

[2]*NRC "Demokritos" INP, Hellas*

[3]*University of Ioannina, Hellas*

[4]*Institute of Nuclear Physics, Krakow, Poland*

[5]*Northeastern University, USA*

[6]*CERN, Geneva, Switzerland*

Abstract

We present results of the performance of the first prototype of the CASTOR quartz-tungsten sampling calorimeter, to be installed in the very forward region of the CMS experiment at the LHC. This study includes GEANT Monte Carlo simulations of the Čerenkov light transmission efficiency of different types of air-core light guides, as well as analysis of the calorimeter linearity and resolution as a function of energy and impact-point, obtained with 20-200 GeV electron beams from CERN/SPS tests in 2003. Several configurations of the calorimeter have been tested and compared, including different combinations of (i) structures for the active material of the calorimeter (quartz plates and fibres), (ii) various light-guide reflecting material (glass and foil reflectors) and (iii) light-sensing devices (photomultipliers and avalanche photodiodes).

1 Introduction

The CASTOR (Centauro And Strange Object Research) detector is a quartz-tungsten sampling calorimeter that has been proposed to study the very forward rapidity (baryon-rich) region in heavy ion collisions in the multi-TeV range at the LHC [1] and thus to complement the heavy ion physics programme, developed essentially in the baryon-free midrapidity region. CASTOR will be installed in the CMS experiment at 14.38 m from the interaction point, covering the pseudorapidity range $5.2 < \eta < 6.6$ and will, thus, contribute not only to the heavy ion program, but also to diffractive and low-x physics in pp collisions [2]. The CMS and TOTEM experiments supplemented by the CASTOR detector will constitute the largest acceptance system ever built at a hadron collider, having the possibility to measure the forward energy and particle flow up to $\eta = 6.6$ [3]. With the design specifications for CASTOR, the total and the electromagnetic energies in its acceptance range (E_{tot} ∼180 TeV and E_{em} ∼50 TeV respectively according to HIJING [4] PbPb simulations at 5.5 TeV) can be measured with a resolution better than ∼1% and, therefore, "Centauro" and/or strangelets events with an unusual ratio of electromagnetic to total (hadronic) energies [5] can be well identified.

A calorimeter prototype has been constructed and tested with electron beams at CERN/SPS in the summer 2003. The purpose of this beam test was to investigate and compare the performance of different component options (structure of the quartz active material, choice of the light guides/reflectors and light sensing devices), rather than to get precise quantitative results of the response of the final detector setup. The general view of the prototype is shown in Figure 1. The different detector configurations considered in this work are shown schematically in Figure 2. Preliminary results of the analysis have been presented at different CMS meetings [6]. Here we present a more quantitative analysis, including the beam profile data [7].

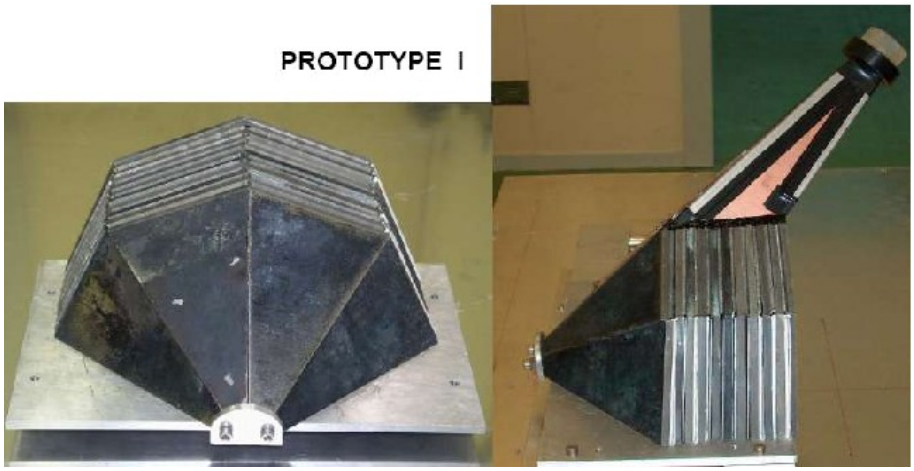

Figure 1: CASTOR prototype I: frontal view (left) and lateral view (right, only one light guide is shown).

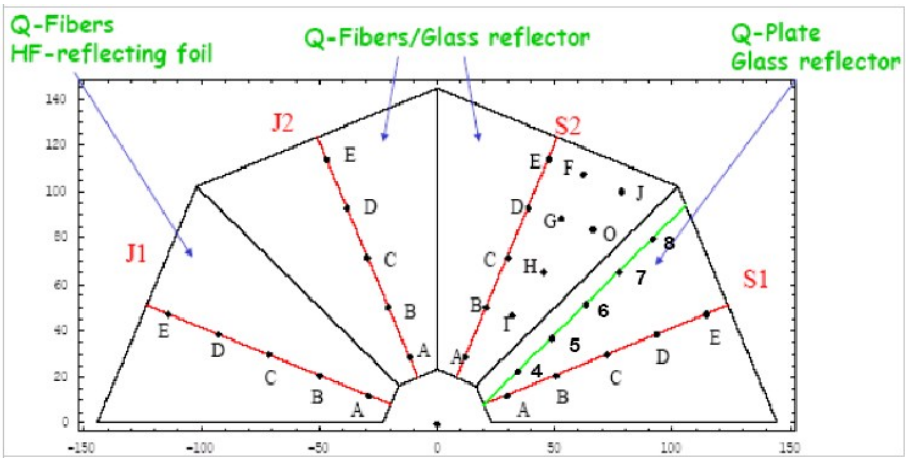

Figure 2: Configuration options investigated in the 2003 beam test: different quartz structures (fibres and plate) and reflectors (glass, foil). The points A-E and 4-8 are scan locations used in calorimeter response uniformity studies (see Section 3.2).

2 Technical description

The CASTOR detector is a Čerenkov-effect based calorimeter with tungsten (W) absorber and quartz (Q) as sensitive material. An incident high-energy particle will shower in the tungsten volume and produce relativistic charged particles that will emit Čerenkov light in the quartz plane. The Čerenkov light is then collected and transmitted to light-sensing devices through air-core light-guides. The different instrumentation options, investigated in this work, are shown in Figure 2. In section 2.1 we describe the various arrangements of the active (quartz) and passive (tungsten) materials of the calorimeter considered. Section 2.2 discusses the light transmission efficiency of different combinations of light-guides and reflectors and section 2.3 summarizes the characteristics of the light-sensing devices (photomultipliers and avalanche photodiodes) tested.

2.1 Tungsten - Quartz

The calorimeter prototype is azimuthally divided into 4 octants and longitudinally segmented into W/Q layers (Fig. 1). Each tungsten absorber layer is followed by a number of quartz planes. The tungsten/quartz planes are inclined at 45° with respect to the beam axis to maximize Čerenkov light output[1)]. The tungsten plates have density $\sim$ 19.0 g/cm^3. The total length of each sector is $0.83\lambda_{int}$, or $23.7X_0$.

The calorimeter response and relative energy resolution were studied for quartz fibres (Q-F) and quartz plates (Q-P) (see Section 3). We have tested four octant readout units of the calorimeter, arranged side-by-side in four azimuthal sectors. Each readout unit consisted of 10 sampling units. Each sampling unit for sectors J1, J2, and S2 (see Fig. 2) is comprised of a 5 mm thick tungsten plate and three planes of 640 μm thick quartz fibres. The quartz fibres were produced by Ceram Optec and have 600 μm pure fused silica core with a 40 μm polymer cladding and a corresponding numerical aperture NA = 0.37. The sampling unit for sector S1 consisted of a 5 mm thick tungsten plate and one 1.8 mm thick quartz plate. Both types of quartz active material, fibre or plate, had about the same effective thickness. The filling ratio was 30% and 37% for the quartz fibres and quartz plates, respectively.

2.2 Air-core light guides

The light guide constructed for the CASTOR prototype I is shown in Figure 3. It is an air-core light-guide made of Cu-plated 0.8 mm PVC. The internal walls are covered either with a glass reflector (AlO+MgFr) or with a reflector foil (Dupont AlO+SiO_2+TiO_2). The light transmittance in the light-guides was studied for both types of reflecting materials.

[1)] The index of refraction of quartz is $n = 1.46 - 1.55$ for wavelengths λ = 600-200 nm. The corresponding Čerenkov threshold velocity is $\beta_c = 1/n = 0.65 - 0.69$, and therefore, for $\beta_c \approx 1$ the angle of emission is $\theta_c = acos(1/n\beta) = 46^\circ - 50^\circ$.

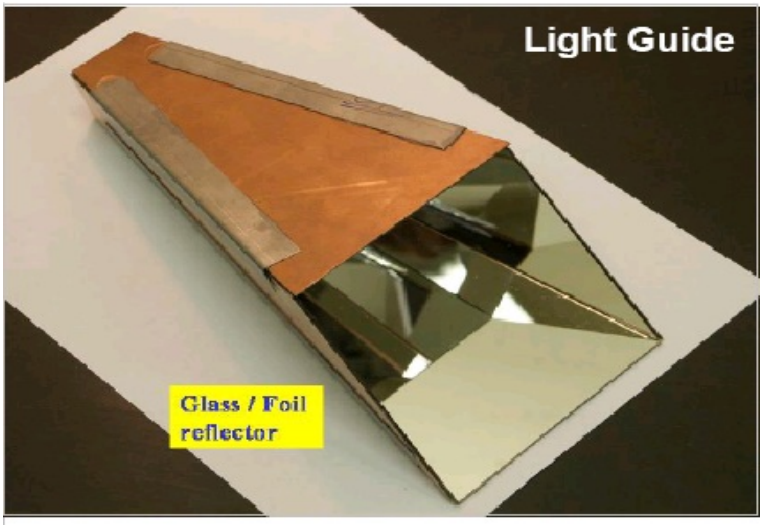

Figure 3: Picture of the light guide used in the prototype.

The design and dimensions of the light guide are obtained from Monte Carlo simulations. In the simulations, the Čerenkov photons produced in the quartz of the calorimeter are collected and transmitted to the light-sensing device by air-core light guides. The efficiency of light transmission and its dependence on the light-source position are crucial parameters characterizing the light guide and significantly affecting the performance of the calorimeter. We developed a GEANT 3.21-based code to simulate the transmission of Čerenkov photons produced in the quartz plane through a light guide [8]. A photon is tracked until it is either absorbed by the walls or by the medium and is thus lost, or until it escapes from the light guide volume. In the latter case it is considered detected only if it escapes through the exit to the light-sensing device. If it is back-scattered towards the entry of the light guide it is also lost.

In the simulations, fibres of various numerical apertures (NA = 0.22 - 0.48) as well as light-guides of various shapes (fully square cross section or partially tapered) were used (see Fig. 4). The maximum values of core-exiting and air-entering angles (θ_{core}, θ_{air}) in degrees for various numerical apertures are given in Table 1. For the quartz plate, the air-entering angle, θ_{air}, is larger than 30°.

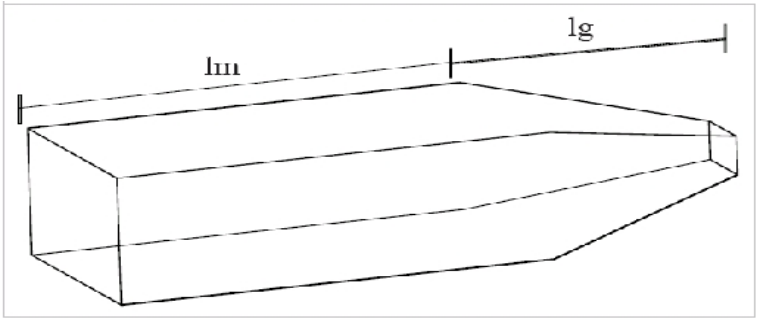

Figure 4: General view of the air-core light guide geometry. *lg* (*lm*) is defined as the ratio of the length of the (non-)tapered section over the mean dimension of the base of the light guide.

Table 1: Maximum values of the core-exiting (θ_{core}) and air-exiting (θ_{air}) angles, for various numerical apertures (NA) of the quartz fibres (index of refraction: n_{core} = 1.46).

NA (n_{core}=1.46)	θ_{core}	θ_{air}
0.22	8.7	12.7
0.37	14.7	21.7
0.40	15.9	23.6
0.44	17.5	26.1
0.48	19.2	28.7

The walls of the simulated light guide have a reflection coefficient of 0.85, simulating the reflecting internal mirror surface of the glass light guide. The entrance plane of the light guide was uniformly scanned with the simulated light source. The percentage of photons escaping in the direction of the light-sensing device has been recorded as a function of the source position, giving, after integration over the complete surface, the light guide efficiency. The spatial uniformity of the light-guide performance can be quantified with the relative variation (σ/mean) of the efficiency across the entrance. Results for the light guides efficiency and uniformity studied are tabulated in Tables 1–5 and are plotted in Figures 5 and 6 for fibres with NA = 0.37 and 0.48, respectively. The parameters *lg* and *lm* refer to the tapered and non-tapered sections of the light guide, as shown in Figure 4, defined as [8]:

lg = length of tapered part over the mean length of entrance, and

lm = length of non tapered part over the mean length of entrance.

Thus, e.g. with an entrance mean length of 10 cm, an lg:lm=1:2 light guide has a total length of 30 cm with 10 cm of tapering part, and an lg:lm=2:0 one is a fully tapered light guide with length 20 cm. In tables 2–5, the row (column) indicates the magnitude of the parameters *lm* (*lg*), respectively.

Table 2: Light-guide efficiency (%) for different values of the *lg* and *lm* parameters (see text) and quartz fibres with NA = 0.37.

$lg \backslash lm$	0	1	2
1	38.3	34.5	34.8
2	46.1	39.1	43.2
3	44.8	41.8	41.5

Table 3: Relative variation of the light-guide efficiency across the entrance, σ/Mean (%), for different values of the *lg* and *lm* parameters (see text) and quartz fibres with NA = 0.37.

$lg \backslash lm$	0	1	2
1	39.3	35.5	3.6
2	8.9	38.3	3.4
3	3.3	22.8	3.2

Table 4: Light-guide efficiency (%) for different values of the *lg* and *lm* parameters (see text) and quartz fibres with NA = 0.48.

lg \ *lm*	0	1	2
1	31.1	28.3	27.1
2	30.1	27.5	27.5
3	27.1	25.0	25.0

Table 5: Relative variation of the light-guide efficiency across the entrance, σ/Mean (%), for different values of the *lg* and *lm* parameters (see text) and quartz fibres with NA = 0.48.

lg \ *lm*	0	1	2
1	20.4	23.8	4.1
2	3.9	28.4	4.6
3	3.8	23.2	3.7

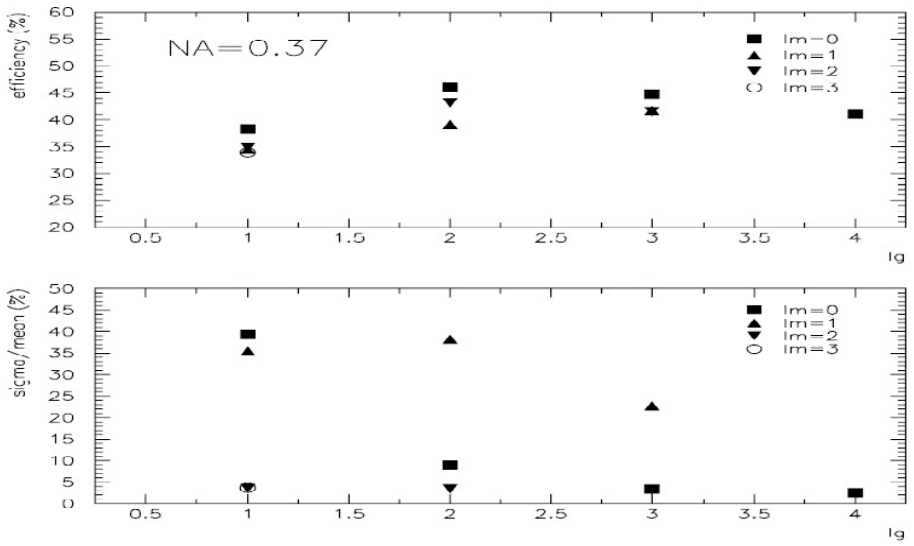

Figure 5: Efficiency (top) and relative variation of the efficiency (bottom) for various light guides (calorimeter quartz fibres with NA = 0.37) for different values of the *lg* and *lm* parameters (see text).

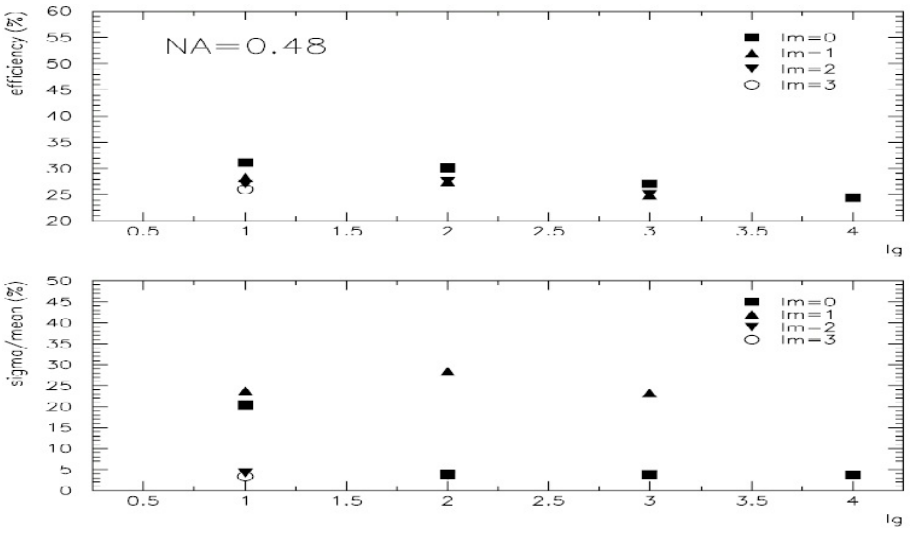

Figure 6: Efficiency (top) and relative variation of the efficiency (bottom) for various light guides (calorimeter quartz fibres with NA = 0.48) for different values of the *lg* and *lm* parameters (see text).

From the tables 1-5 and figures 5 and 6 we note that, as the NA of the fibre and hence the air-entering angle, θ_{air}, increases, the transmission efficiency decreases. Also, the optimum length for the air-core light guide decreases, while the uniformity of the light exiting increases.

We have considered two alternatives for the reflecting medium in the light guide:

1. 0.5 mm thick float-glass with evaporations of AlO and MgFr, Fig. 7a, and
2. Dupont polyester film reflector coated with AlO and reflection enhancing dielectric layer stack SiO_2+TiO_2, the so-called HF reflector foil, Fig. 7b.

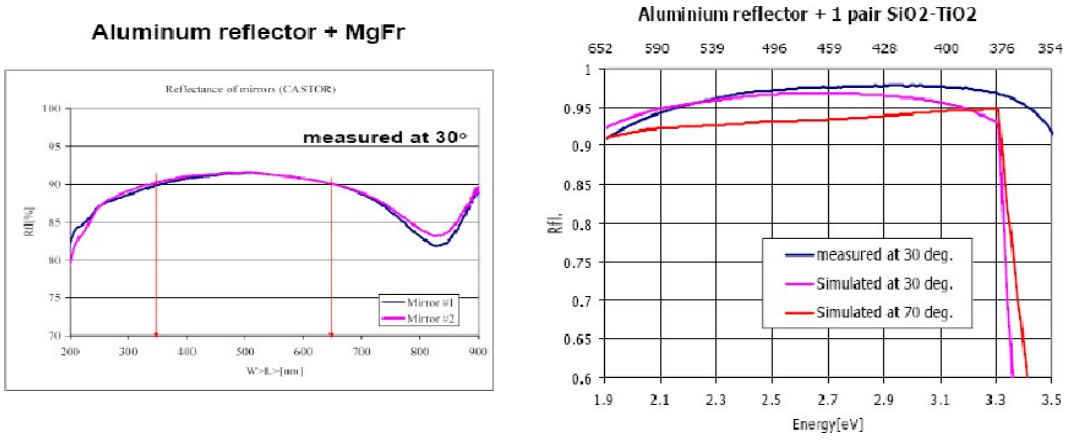

Figure 7: Reflectance of two mirrors coated with (a) AlO+MgFr and (b) Dupont foil with AlO and SiO_2+TiO_2, as a function of the incident light wavelength.

To choose the most suitable reflector, we also have to take into account the quantum efficiency of the light-sensing device (see Section 2.3) This is because the short wavelength Čerenkov light ($\lambda < 400$ nm) deteriorates fast with irradiation of the quartz material and thus a continuous compensation must be applied. The optimum combination of the reflector and the Q-efficiency of the light-sensing device ensure that the total efficiency is maximized above

400 nm and falls sharply to zero below 400 nm. In Table 6 we calculate the product of the light guide transmittance and APD quantum efficiency for Q-fibres with NA = 0.37 and 3 internal reflections in the designed light guide.

Table 6: Light guide transmittance times the Avalanche Photodiode quantum efficiency at each wavelength (see Figure 9) for the two reflectors and quartz fibres (Q-F: NA = 0.37, 3 reflections).

Wavelength	Glass reflector (Al+MgF)	Dupont + Layer stack
650 nm	62%	64%
400 nm	53%	62%
350 nm	44%	7%
300 nm	10%	$\sim$0%

2.3 Light-sensing Devices

We instrumented the calorimeter prototype with two different types of light-sensing devices:

1. Two different kinds of Avalanche Photodiodes (APDs): Hamamatsu S8148 (APD1) and Advanced Photonics DUV (APD2), Fig. 8.

2. Two different types of photomultipliers (PMTs): Hamamatsu R374 and Philips XP2978.

We used 4 Hamamatsu APDs, each 5×5 mm^2, in a 2×2 matrix with total area of 1 cm^2. The Advanced Photonics DUV APD had an active area of 2 cm^2, (ϕ=16 mm). The Hamamatsu and Philips PMTs have both an active area of 3.1 cm^2. The Hamamatsu and Advanced Photonics APD quantum efficiency are shown versus wavelength in Fig. 9.

Figure 8: Two types of APDs used in the beam test.

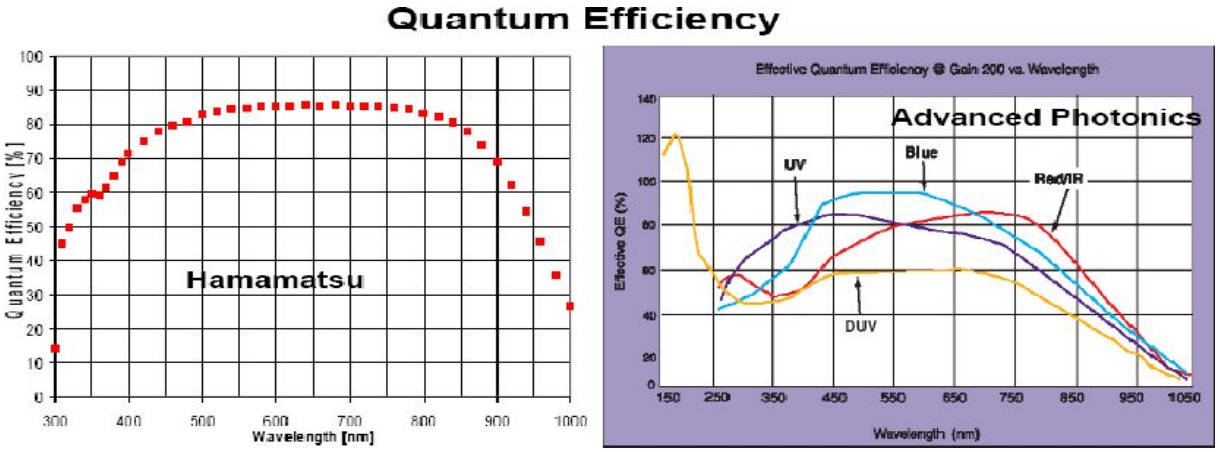

Figure 9: The Hamamatsu and Advanced Photonics APD quantum efficiency versus wavelength.

3 Beam Test Results

The beam test took place in summer 2003 at the H4 beam line of the CERN SPS. The calorimeter prototype was placed on a platform movable with respect to the electron beam in both horizontal and vertical (X,Y) directions. Telescopes of two wire chambers, as well as two crossed finger scintillator counters, positioned in front of the calorimeter, were used to determine the electron impact point. In the next two sections we present the measured calorimeter linearity and resolution as a function of energy and impact point for different prototype configurations.

3.1 Energy Linearity and Resolution

To study the linearity of the calorimeter response and the relative energy resolution as a function of energy, the central points C (Fig. 2) in different azimuthal sectors have been exposed to electron beams of energy 20, 40, 80, 100, 150 and 200 GeV. The results of the energy scanning, analyzed for four calorimeter configurations, are shown in figures 10–13. The distributions of signal amplitudes, after introducing the cuts accounting for the profile of the beam, are in most cases symmetric and well fitted by a Gaussian function. Asymmetry in few distributions was partly caused by the wide spread of the beam in these events.

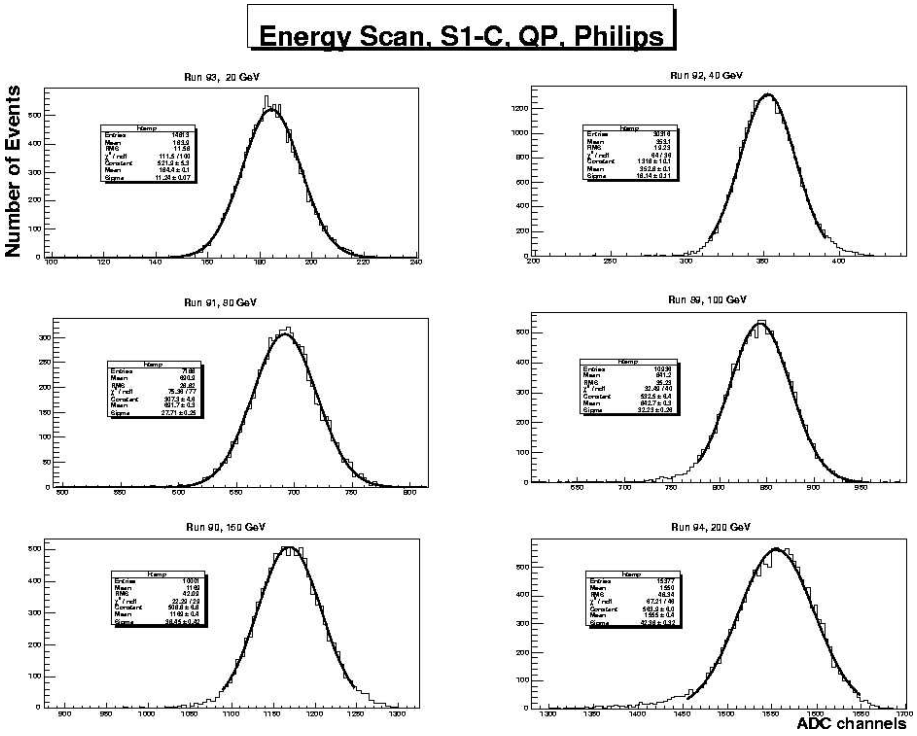

Figure 10: Distributions of signal amplitudes in ADC channels for electron beam energies (20, 40, 80, 100, 150 and 200 GeV) impinging on the central point C of sector S1 (Philips PMT).

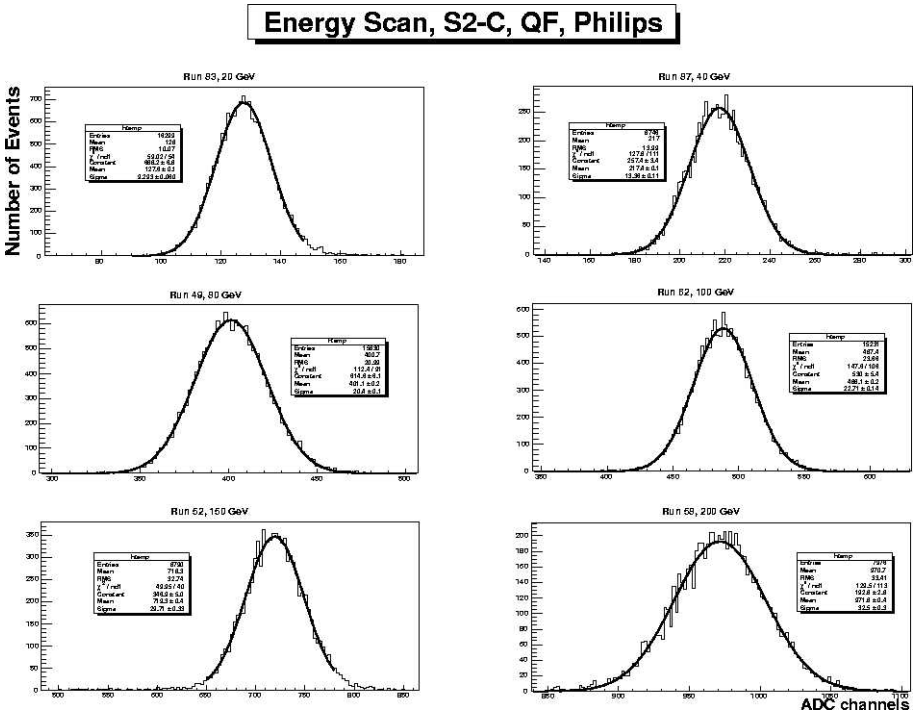

Figure 11: Distributions of signal amplitudes in ADC channels for electron beam energies (20, 40, 80, 100, 150 and 200 GeV) impinging on the central point C of sector S2 (Philips PMT).

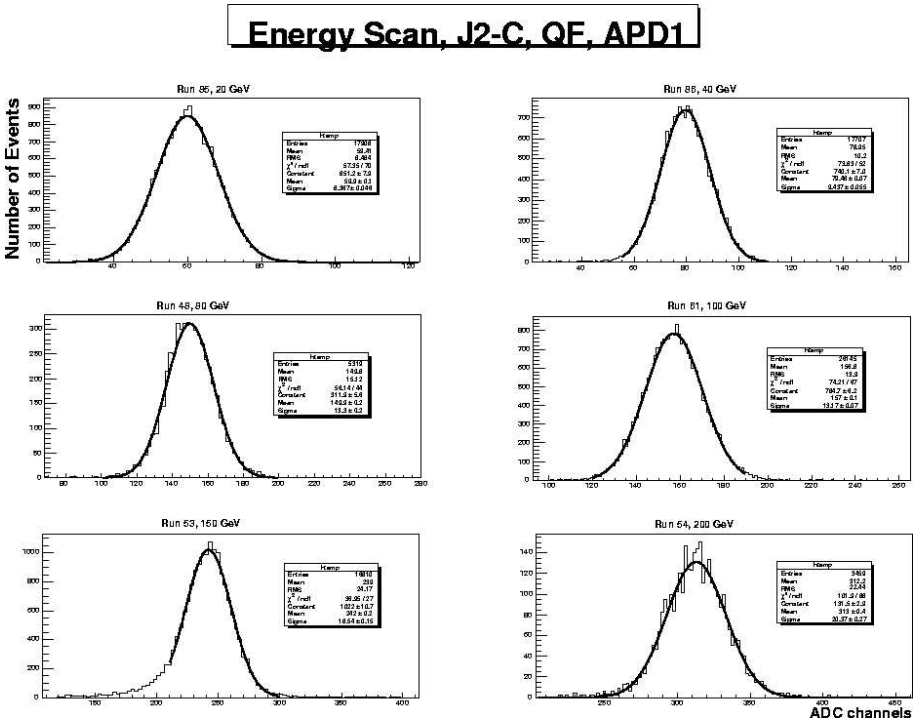

Figure 12: Distributions of signal amplitudes in ADC channels for electron beam energies (20, 40, 80, 100, 150 and 200 GeV) impinging on the central point C of sector J2 (Hamamatsu APD).

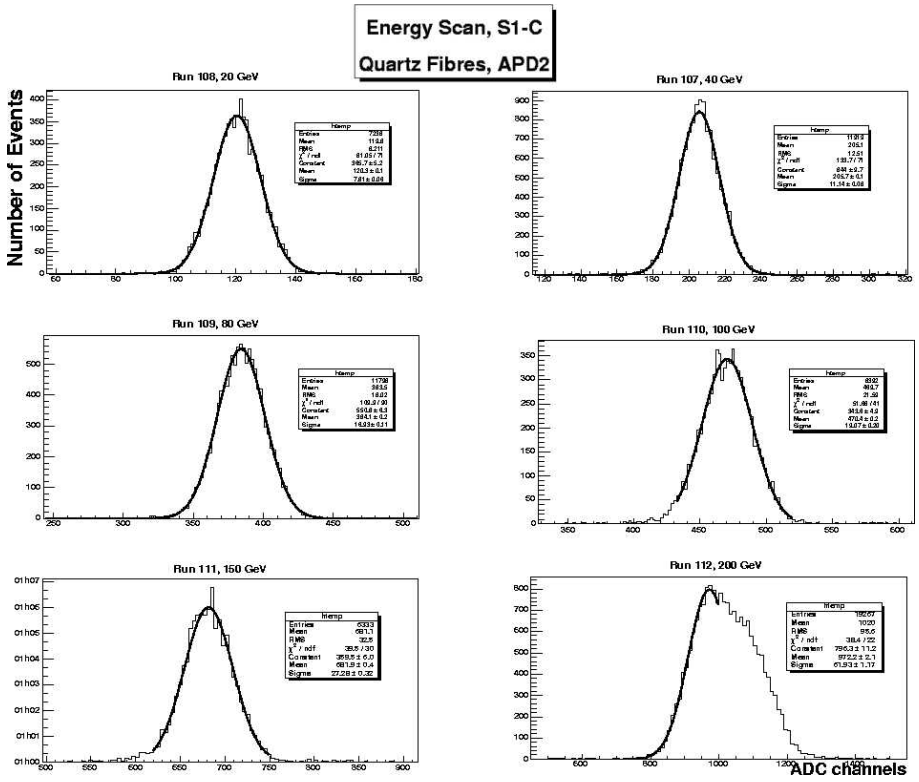

Figure 13: Distributions of signal amplitudes in ADC channels for electron beam energies (20, 40, 80, 100, 150, and 200 GeV) impinging on the central point C of sector S1 (Advanced Photonics APD).

For all configurations, the calorimeter response is found to be linear in the energy range explored (see Fig. 14). The average signal amplitude, expressed in units of ADC channels, can be satisfactorily fitted by the following formula:

$$ADC \quad = \quad a + b \times E \tag{1}$$

where the energy E is in GeV. The ADC distributions are not pedestal subtracted (the *a* parameter gives the pedestal value which is roughly the same for all studied configurations). The fitted values of the parameters for each configuration are shown in Fig. 14 and are tabulated in Table 7.

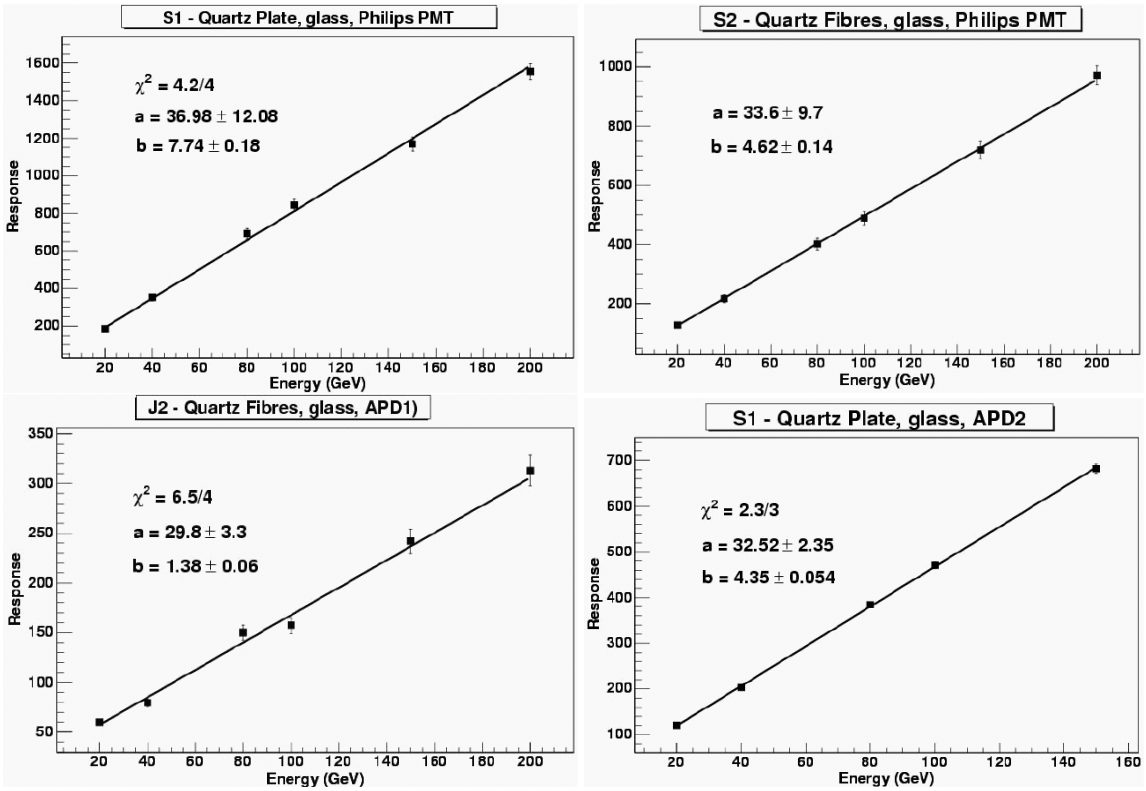

Figure 14: Energy linearity in sectors: (a) S1 (Philips PMT), (b) S2 (Philips PMT), (c) J2 (APD1), (d) S1 (APD2).

The relative energy resolution of the calorimeter has been studied by plotting the normalized width of the Gaussian signal amplitudes (Figs. 10– 13), σ/E, with respect to the incident beam electron energy, E (GeV) and fitting the data points with two different functional forms [9]:

$$\sigma/E = p_0 + p_1/\sqrt{E} \quad (2)$$

$$\sigma/E = p_0 \oplus p_1/\sqrt{E} \oplus p_2/E \quad (3)$$

where the $\oplus$ indicates that the terms have been added in quadrature. In expression (3), three terms determine the energy resolution:

1. The constant term p_0, coming from the gain variation with changing voltage and temperature, limits the resolution at high energies.
2. The stochastic term p_1, due to intrinsic shower photon statistics, and
3. the p_2 term, which contains the noise contribution from capacitance and dark current.

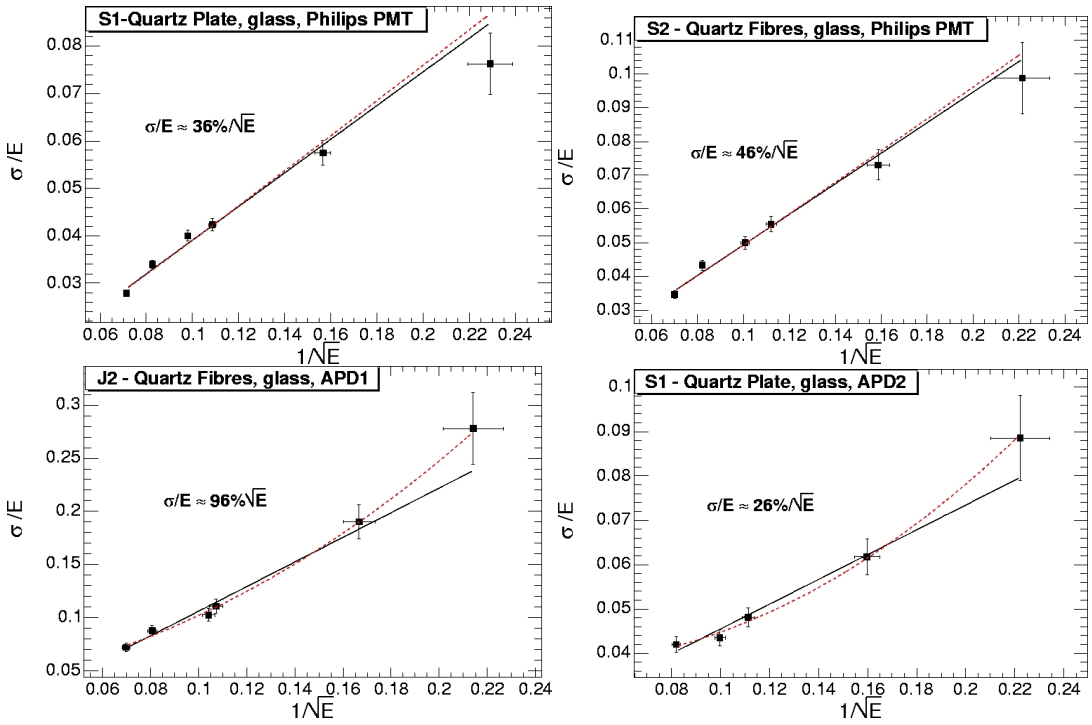

Figure 15: Energy resolution in sectors: (a) S1 (Philips PMT), (b) S2 (Philips PMT), (c) J2 (APD1), (d) S1 (APD2). Two fits are shown: $\sigma/E = p_0 + p_1/\sqrt{E}$ (black); $\sigma/E = p_0 \oplus p_1/\sqrt{E} \oplus p_2/E$ (red).

Generally, both formulae satisfactorily fit the data (Fig. 15). The fit parameters are shown in Table 7. The first thing to notice is that the constant term p_0 is close to 0 for all options. The measured stochastic term p_1 is in the range $\sim$ 24% - 82% and indicates that we may measure the total electromagnetic energy hitting CASTOR in Pb+Pb collisions at the LHC ($\sim$ 40 TeV, HIJING [4] prediction) with a resolution better than 0.3%. The readout by avalanche photodiodes leads to the p_2 term, measured to be 1.25 GeV and 4.5 GeV for Advanced Photonics APD and Hamamatsu APD, respectively. It should be noted that the APDs are very sensitive to both voltage and temperature changes, but in this test there was no such stabilization. In Table 7 we summarize the fit parameters for both parameterizations and for the four considered configurations.

Table 7: Energy linearity and resolution of four different configurations of the CASTOR calorimeter prototype. For the energy resolution, we quote the parameters for two fits: (1) $\sigma/E = p_0 + p_1/\sqrt{E}$, and (2) $\sigma/E = p_0 \oplus p_1/\sqrt{E} \oplus p_2/E$.

		RESOLUTION				LINEARITY		
	fit	p_0	p_1	p_2 [GeV]	χ^2/ndf	a	b	χ^2/nd
Quartz Plate **S1, glass**								
Philips PMT	1	0.004 ± 0.002	0.36 ± 0.02		6.4/4	37.0 ± 12.1	7.74 ± 0.18	4.2/4
	2	0.010 ± 0.004	0.38 ± 0.02	0.00 ± 0.42	7.4/3			
Advanced Photonic APD	1	0.017 ± 0.005	0.28 ± 0.04		2.5/3	32.5 ± 2.4	4.35 ± 0.05	2.2/3
	2	0.036 ± 0.006	0.21 ± 0.01	1.25 ± 0.20	6.2/2			
Quartz Fibres **S2, glass** Philips PMT	1	0.004 ± 0.003	0.45 ± 0.04		3.2/4	33.6 ± 9.7	4.6 ± 0.1	0.41/4
	2	0.013 ± 0.006	0.48 ± 0.02	0.00 ± 0.83	3.7/3			
Quartz Fibres **J2, glass** Hamamatsu APD	1	-0.01 ± 0.01	1.16 ± 0.13		4.1/4	29.8 ± 3.3	1.38 ± 0.06	6.5/4
	2	0.04 ± 0.02	0.82 ± 0.22	4.5 ± 1.6	1.3/3			

3.2 Area scanning

The purpose of the area scanning was to check the uniformity of the calorimeter response, affected by electrons hitting points at different places on the sector area, as well as to assess the amount of "edge effects" and lateral leakage from the calorimeter, leading to cross-talk between neighboring sectors.

For the area scanning of sector S2, connected to the Philips PMT, central points (A-E) as well as border points (I-O) have been exposed to electron beam of energy 100 GeV (see Fig. 2). The distributions are symmetric and well described by Gaussian fits for the majority of the points. Asymmetric distributions are seen only for points closer than $\sim$3 mm to the calorimeter outer edge or sector border.

Figure 16 shows the calorimeter response and relative resolution (σ/E) as a function of the distance R from the calorimeter center, for both central and border points. The top plot shows the coordinates of the points, corrected for the beam impact point position. It is seen that points E, F, J practically lie at the upper edge of the calorimeter. The rise of the signal amplitudes (bottom left), as well as of the distribution widths with R can be attributed to a lateral spread of the beam. For large R, a substantial part of the electron beam is outside of the calorimeter sector and falls directly onto the light guides. The bottom right plot shows that the energy resolution is $\sim$ 4.7% for 100 GeV electrons and is relatively independent of the position of the impact points.

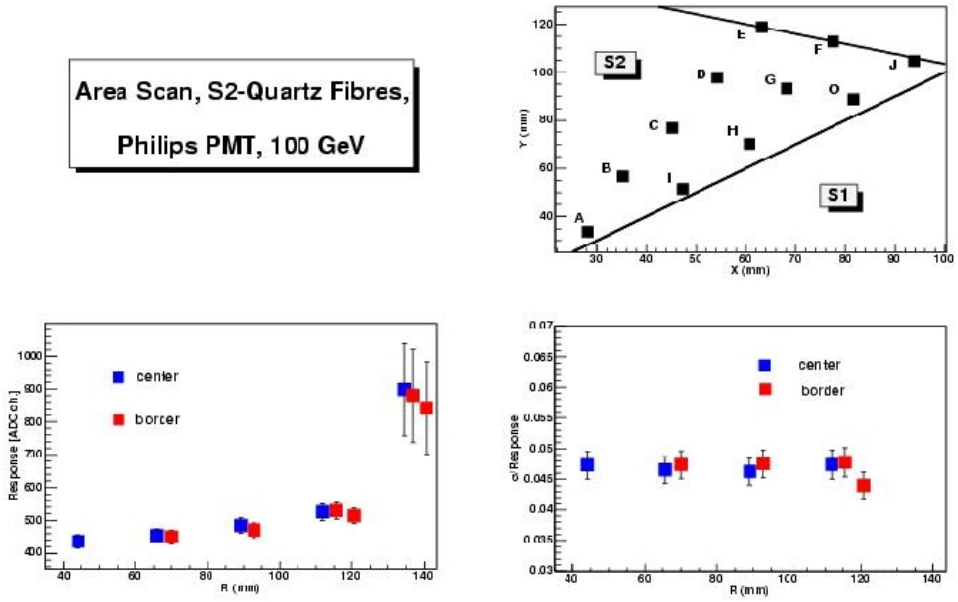

Figure 16: Dependence of signal amplitude on the distance R from the calorimeter center in sector S2 (Philips PMT). Top: Coordinates of the scanned points. Bottom plots: Measured response to 100 GeV electrons on central (A-E, blue) and border (I-O, red) points.

3.2.1 S1 - S2 cross talk

Ten points, located at distances 2.5-32 mm from the S1/S2 sector border, have been exposed to the electron beam of energy 80 GeV. The simultaneous readout of both sectors has been done by Advanced Photonics APD and Hamamatsu PMT in S1 and S2, respectively. The upper left pad of Figure 17 shows the coordinates of the measured points in the calorimeter frame, corrected for the beam impact point position. The star symbol marks the coordinates of the border point between S1 and S2 sectors, found from the dependence of the signal amplitudes on X(Y) coordinates (lower pads).

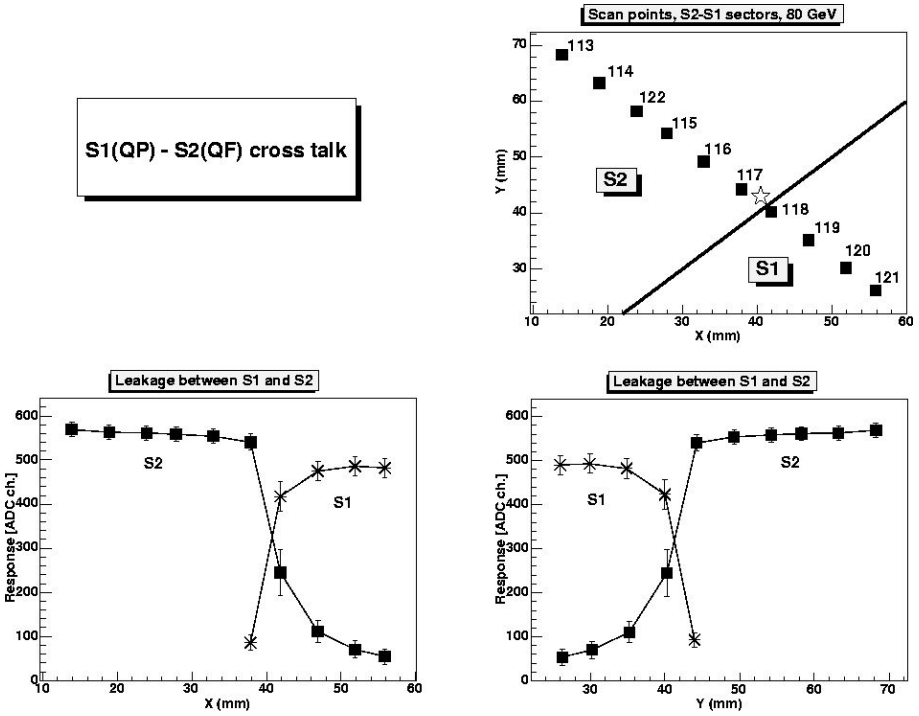

Figure 17: Top: Position of the points in the calorimeter frame, corrected for the beam impact points. Bottom: Measured calorimeter response versus coordinates X (left) and Y (right) in sectors S1 (APD2) and S2 (Hamamatsu PMT) for several points at distances $\sim$ 2.5-32 mm from the sector border.

The distributions of the signal amplitudes in S2 sector, for points distanced from the sector border more than $\sim$ 8 mm, are symmetric (Gaussian) and leakage to S1 sector is negligible. The relative energy resolution σ/E is of the order $\sim$ 2.9% for 80 GeV electrons.

The dependence of the calorimeter response, leakage fraction and relative energy resolution, σ/response, on the distance *d* from the sector border, for S1 and S2 sectors are shown in Figure 18.

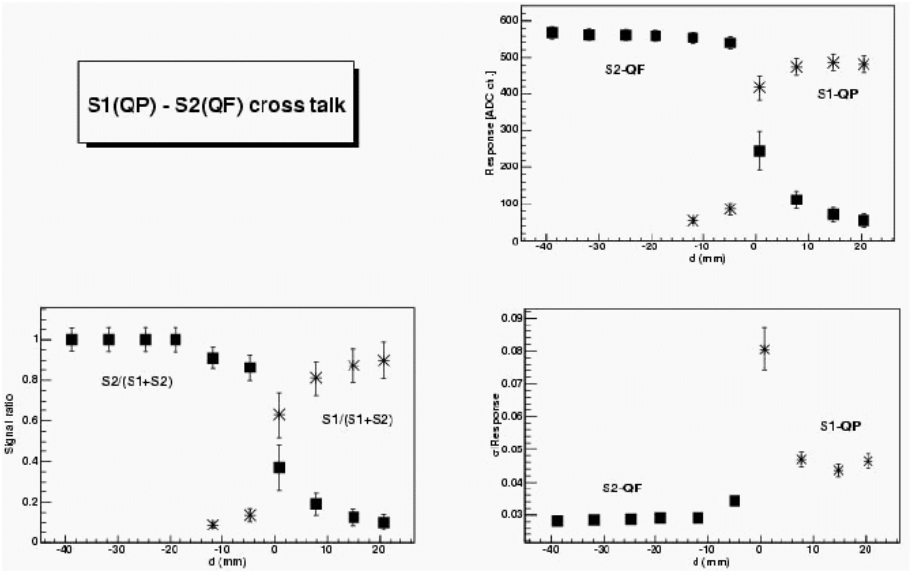

Figure 18: Comparison of the calorimeter response (top right), leakage fraction (bottom left), and relative energy resolution, σ/response, (bottom right) in sectors S1 (APD2) and S2 (Hamamatsu PMT) for points at different distances *d* from the sector border.

Both the light output and energy resolution are a little better for S2 sector, connected to Hamamatsu PMT ($\sigma/E \sim$ 2.9%), than for S1 sector, connected to Advanced Photonics APD ($\sigma/E \sim$ 4.5%). This is expected since there is more light collected by the PMT as compared to the APD: area(PMT)/area(APD) = 1.55.

3.2.2 Comparison of J1, J2 and S1 sectors

For comparison of the uniformity of calorimeter response, several points located at different places on the sectors have been exposed to the electron beam of 80 GeV energy. The points (A-E) at the middle of J1, J2 and S1 sectors and points (4-8) at the border of S1 sector have been studied (see Figure 2). All sectors have been connected to Hamamatsu PMT. Symmetric and Gaussian distributions of signal amplitudes in the middle of the sectors and asymmetric distributions close to the sector border (points 4-8) and sometimes also close to the inner (point A) and outer (point E) calorimeter edge in J1 sector are observed. The beam profile correction reduces the asymmetry.

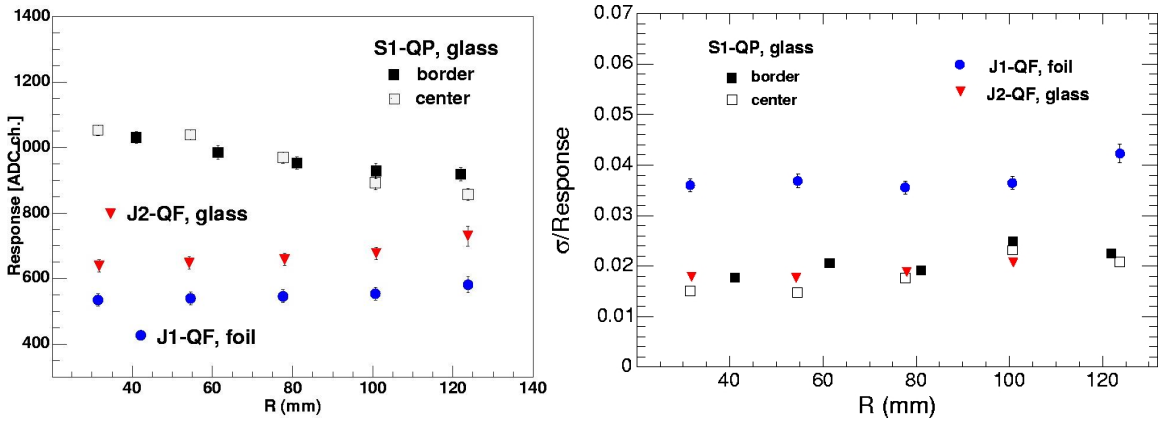

Figure 19: Comparison of calorimeter response (left) and resolution (right) to 80 GeV electrons for several impact points (A-E) of J2, J1 and S1 sectors, readout with Hamamatsu PMTs.

Comparison of light output and relative energy resolution for all options studied is shown in Figure 19. Light output is highest in the S1 (QP-glass) sector and it is practically the same for the central and border points. It depends weakly on the distance *R* of the impact point. For S1, a weak decrease and for J1 and J2 sectors a weak increase of the calorimeter response with distance R from the calorimeter center are observed. The relative energy resolution is almost independent of the position of the impact point and it is $\sim$ 1.5-2.5 % for S1 (QP-glass) and J2 (QF-glass) sectors and $\sim$ 3.5-4.0 % for J2 (QF-foil) for 80 GeV electrons.

4 Summary

We have presented a comparative study of the performances of the first prototype of the CASTOR quartz-tungsten calorimeter of the CMS experiment using different detector configurations. GEANT-based MC simulations have been employed to determine the Čerenkov light efficiency of different types of air-core light guides and reflectors. Electron beam tests, carried out at CERN SPS in 2003, have been used to analyze the calorimeter linearity and resolution as a function of energy and impact point. Different sectors of the calorimeter have been setup with various quartz active materials and with different light-sensing devices (PMTs, APDs). The main results obtained can be summarized as follows:

1. Comparison between the calorimeter response using a single quartz plate or using a quartz-fibre bundle indicates that:

1.a. Good energy linearity is observed for both active medium options (Fig. 14).

1.b. The Q-plate gives more light output than equal thickness Q-fibres (Fig. 19).

1.c. Relative energy resolution is similar for quartz plates and quartz fibres (Fig. 15). When readout with the same Hamamatsu PMT (S1, S2 sectors), we found $\sim$2% energy resolution for 80 GeV electrons (Fig. 19).

1.d. The constant term p_0 of the energy resolution, that limits performance at high energies, is less than 1% in both options for the same Philips PMT and glass reflector (Fig. 15). The stochastic term p_1 is $\sim$36 % and $\sim$46% for quartz plates and quartz fibres, respectively (Table 7).

2. Avalanche-photodiodes (APDs) appear to be a working option for the light-sensing device, although they still need more investigation (radiation-hardness, cooling and voltage stabilization tests).

3. The relative energy resolution is weakly dependent on the position of the impact point (Fig. 19). Leakage (cross-talk) between sectors is negligible for impact points separated more than 8 mm from the sector border. Only, electrons impinging less than 3 mm from the detector edge show a degraded energy response and worse resolution.

4. The light output is a little higher for the light-guides with glass reflector compared to those that use HF-foil, for the same light sensing device (Hamamatsu PMT, Fig. 19). This is understood, since the HF reflecting foil is designed to cut Čerenkov light with $\lambda < 400$ nm, where the light output is greater. However, the HF-reflector foil has higher efficiency in the region $\lambda > 400$ nm than the glass mirror (Table 6).

In summary, this study suggests that equipping the CASTOR calorimeter with quartz-plates as active material, APDs as light-sensing devices (with temperature and voltage stabilization), and light-guides with foil reflector is a promising option, although the final configuration would benefit from some further (detailed) investigation to take into account the experimental conditions that will be encountered in the forward rapidity region of CMS. A beam test of the second prototype is foreseen for 2004.

5 Acknowledgments

We wish to thank R. Wigman and N. Akchurin for assistance in the early stage of the beam test. This work is supported in part by the Secretariat for Research of the University of Athens and the Polish State Committee for Scientific Research (KBN) SPUB-M nr. 620/E-77/SPB/CERN/P-03/DWM 51/2004-2006. DdE acknowledges support by the 6th EU Framework Programme (contract MEIF-CT-2005-025073).

References

[1] A.L.S. Angelis and A.D. Panagiotou, J.Phys.G23:2069-2080,1997; A.L.S. Angelis *et al*., hep-ex/9901038; A.L.S. Angelis *et al*., Nucl.Phys.Proc.Suppl. 97:227-230,2001.

[2] A.L.S. Angelis, 3rd CMS Workshop on Forward Physics, CERN, 29-30 May 2002. A.D. Panagiotou, CMS/TOTEM meeting on Diffraction, CERN, 6 December 2002.

[3] K. Eggert, Meeting on Physics at LHC, Prague 6-12, July 2003; Nucl. Phys. B122 (2003) 447.

[4] M. Gyulassy and X.-N. Wang, Phys. Rev. **D44**, 3501 (1991); Comp. Phys. Comm. **83**, 307 (1994).

[5] E. Gladysz-Dziadus, Phys. Part. Nucl. **34**, 285 (2003), hep-ph/0111163.

[6] A.D. Panagiotou, CMS-CPT Week, PRS-HI meeting, November, 2003; and CMS-HF meeting, CMS Week, Sept., 2003, CERN. See `http://cmsdoc.cern.ch/castor/Talks/Talks.html`

[7] E. Gladysz-Dziadus, Institute Nuclear Physics, PAN, Krakow, Report # 1942PH-2004. See `http://www.ifj.edu.pl/`

[8] G. Mavromanolakis, A.L.S. Angelis, A.D. Panagiotou, ALICE/CAS-2000-20. See `http://cmsdoc.cern.ch/castor/biblio/bibliotxt/Notes.html`

[9] G. Anvinzino *et al.*, Meth. Phys. Res. A357(1995)369; M. Livan, V. Vercesi and R. Wigmans, CERN 95-02, 1995.